

Decoupled hot gas flows in elliptical galaxies

S. Pellegrini¹ and L. Ciotti²

¹Dipartimento di Astronomia, Università di Bologna, via Zamboni 33, 40126 Bologna, Italy

²Osservatorio Astronomico di Bologna, via Zamboni 33, 40126 Bologna, Italy

Received ... ; accepted ...

Abstract. We present the results of a new set of hydrodynamical simulations of hot gas flows in model elliptical galaxies with the following characteristics: the spatial luminosity distribution approaches a power law form at small radii, in accordance with the results of recent ground based observations, and with the Hubble Space Telescope; the dark matter has a peaked profile too, as indicated by high resolution numerical simulations of dissipationless collapse; the dark to luminous mass ratio spans a large range of values, including low values found by optical studies confined to within two effective radii; finally, the type Ia supernova rate is that given by the latest estimates of optical surveys, or zero, as suggested by the iron abundances recently measured in the hot gas.

We find that the resulting gas flows are strongly decoupled: an inflow develops in the central region of the galaxies, while the external parts are still degassing, i.e., the flows are mostly partial winds. This behavior can be explained in terms of the local energy balance of the hot gas. A large spread in the X-ray luminosity L_X at fixed optical luminosity L_B can be produced as in previous simulations that used King models plus massive quasi-isothermal dark halos, and higher supernova rates; the key factor causing large L_X variations is now the size of the central inflow region. The highest L_X observed correspond to global inflows. Finally, non negligible amounts of cold gas can be produced by the partial winds; this could be an explanation for the possible discovery of cold matter at the center of elliptical galaxies, an alternative to the presence of a steady state cooling flow.

Key words: Galaxies: elliptical and lenticular, cD – Galaxies: ISM – Galaxies: kinematics and dynamics – X-rays: galaxies

1. Introduction

X-ray observations, beginning with the *Einstein* Observatory, have demonstrated that normal early-type galaxies are X-ray emitters, with 0.2–4 keV luminosities ranging from $\sim 10^{40}$ to $\sim 10^{43}$ erg s⁻¹ (Fabbiano 1989; Fabbiano, Kim, & Trinchieri 1992). The X-ray luminosity L_X is found to correlate with the blue luminosity L_B ($L_X \propto L_B^{2.0 \pm 0.2}$), but there is a large scatter of roughly two orders of magnitude in L_X at any fixed $L_B > 3 \times 10^{10} L_\odot$ (Fig. 1). The observed X-ray spectra of galaxies with high L_X/L_B ratios are consistent with thermal emission from hot, optically thin gas, while those of low L_X/L_B objects can be mostly accounted for by emission from stellar sources (Kim, Fabbiano, & Trinchieri 1992).

The scatter in the $L_X - L_B$ diagram has been recognized as the most striking feature of the X-ray properties of early-type galaxies. Using new apparent magnitudes and fundamental plane distances, it was shown that this scatter is reduced by 20%, but not eliminated (Donnelly, Faber & O’Connell 1990; see Fig. 1b). This result is based on the old estimate of the X-ray fluxes (that of Canizares, Fabbiano, & Trinchieri 1987), and on just half of the final sample of X-ray galaxies produced by Fabbiano et al. 1992 (see Eskridge, Fabbiano & Kim 1995 for a detailed comparison of the statistical results by Donnelly et al. with those obtained using the whole sample). One can argue that the large dispersion in L_X is definitively not the result of distance errors on the basis of the fact that a scatter of the same size as in Fig. 1a is present even in the distance-independent diagram of L_X/L_B versus the central stellar velocity dispersion (e.g., Eskridge et al. 1995).

Many theoretical models were developed to explain the findings above, including numerical simulations of the behavior of gas flows fed by stellar mass loss and heated by type Ia supernovae (SNIa). Steady state cooling flow models were investigated first (Nulsen et al. 1984, Sarazin & White 1987,1988), and it was found that these can only reproduce X-ray bright galaxies. Evolutionary models with a SNIa rate approximately constant with time have been carried out by Mathews & Loewenstein (1986), Loewenstein & Mathews (1987), and David, Forman, &

Jones (1990, 1991). After a very brief initial wind phase, driven by the explosion of type II supernovae, the resulting flow evolution goes from a global inflow to a wind, which is experienced only by the smallest galaxies by the present time. David et al. (1991) conclude that all galaxies above $L_B \simeq 3 \times 10^{10} L_\odot$ host a cooling flow. So, as in the steady state cooling flow scenario, the scatter in L_X at fixed L_B has to be explained by a combination of environmental differences (White & Sarazin 1991) and by large variations from galaxy to galaxy in the stellar mass loss rate per unit L_B , the efficiency of thermalization of the stellar mass loss, and that of thermal instabilities in the hot gas. An alternative way of explaining the scatter in the $L_X - L_B$ diagram is given by the evolutionary scenario of D’Ercole et al. (1989), and Ciotti et al. (1991, C DPR). Assuming that the SNIa explosion rate is declining with time slightly faster than the rate with which mass is lost by the stars, in the beginning the energy released by SNIa’s can drive the gas out of the galaxies through a supersonic wind. As the collective SNIa energy input decreases, a subsonic outflow takes place, which gradually slows until a central cooling catastrophe leads to the onset of an inflow. At fixed L_B , any of the three phases wind, outflow or inflow can be found at the present epoch, depending only on the various depths and shapes of the potential well of the galaxies. In this way both the large scatter in L_X and the trend in the spectral properties are accounted for at the same time: in the X-ray bright galaxies the soft X-ray emitting gas dominates the emission, being in the inflow phase, that resembles a cooling flow; in the X-ray faint galaxies the hard stellar emission dominates, these being in the wind phase.

Recent *ASCA* observations seems to indicate that the SNIa’s activity is suppressed in early-type galaxies, which implies that the C DPR scenario is essentially ruled out. Since this issue is far from closed (§1.3), it is still worthwhile to explore the effects of SNIa’s on the flows, using the updated rate given by recent optical surveys; this is lower than that adopted by C DPR, which was 0.67 the standard one estimated by Tamman (1982). This aspect, together with the need for changes in other galaxy properties crucial for the evolution of hot gas flows, are discussed below.

1.1. New stellar density profiles

Previous numerical simulations of hot gas flows used the King (1972) stellar density distribution mainly for computational ease. This distribution has an inner region of constant density (the so called “core”) of the order of a few hundred parsecs, which keeps the time step of the numerical simulation reasonably small (a stellar density increase implies a reduction of the characteristic hydrodynamical time step). Another advantage of density profiles with a constant density core is that the central regions can be resolved using a larger grid size; this again allows

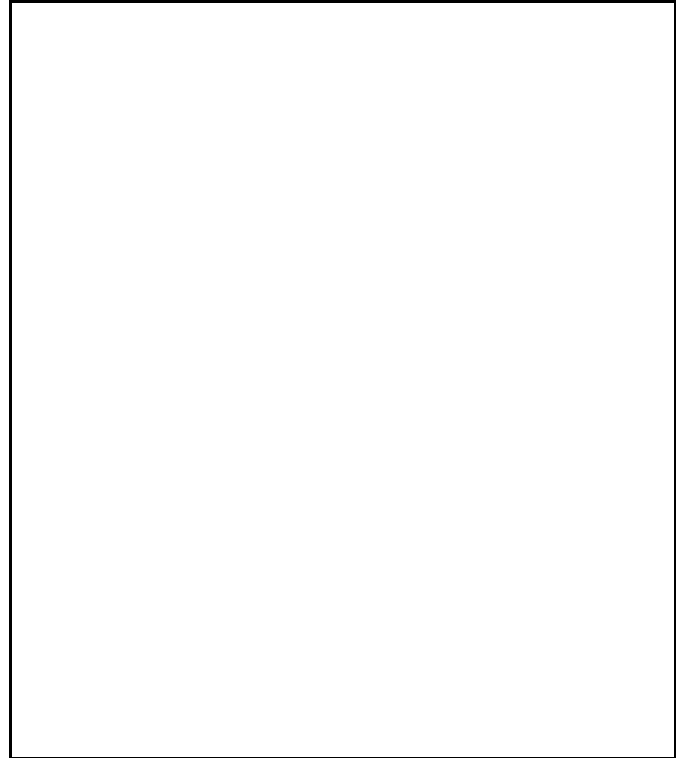


Fig. 1. The $L_X - L_B$ diagram of early-type galaxies with X-ray emission detected by the *Einstein* satellite; X-ray fluxes are from the final catalog of Fabbiano et al. (1992). Apparent B magnitudes and distances are from Fabbiano et al. (1992) in Fig. 1a, and from Donnelly et al. (1990) in Fig. 1b (see Section 1). The dashed line gives an estimate for the stellar source contribution to L_X (from Kim et al. 1992). Also shown with triangles are the positions of the models calculated here (see Section 3.5), to which the stellar source contribution has been added.

a larger time step (see C DPR for a more quantitative discussion). It is well known though that a much better description of the surface brightness profiles of ellipticals is given by the de Vaucouleurs (1948) law. A very good fit to this law is given by the Jaffe (1983) and by the Hernquist (1990) distributions, that have the advantage that all their dynamical properties can be expressed analytically. These distributions belong to the family of the so called γ -models, that has been widely explored recently (Dehnen 1993; Tremaine et al. 1994):

$$\rho(r) = M \frac{(3 - \gamma)}{4\pi} \frac{r_c}{r^\gamma (r_c + r)^{4-\gamma}}. \quad (1)$$

The density profile of the Hernquist law has $\gamma = 1$, while that of the Jaffe law has $\gamma = 2$. Inside r_c the density of γ -models increases as $r^{-\gamma}$, a significant difference with respect to King models: over a few hundreds of parsecs at the center the γ -models are power laws. The existence of cores of constant surface brightness has been definitively ruled out by ground based observations (Lauer 1985, Ko-

rmendy 1985), and recently by the Hubble Space Telescope (Jaffe et al. 1994; Lauer et al. 1995), that has shown how the central surface brightness profile is described by a power law as far in as can be observed, i.e., ~ 10 pc in Virgo. From the point of view of a very accurate photometry, the surface brightness law implied by eq. (1) cannot reproduce well both the envelope and the very center of all the ellipticals observed by HST. The Jaffe law, though, gives a general description of ellipticals accurate enough for the treatment of hot gas flows, on the scales that are relevant for the problem (from a few tens to several thousands of parsecs).

1.2. New dark matter estimates and distributions

Attempts to estimate the amount of nonluminous mass in elliptical galaxies have been made recently through extensive searches for dynamical evidence of dark matter, either with systematic observations of ionized gas probing the gravitational field (Pizzella et al. 1997) or with measurements of stellar velocity dispersions profiles out to large radii (e.g., Bertin et al. 1994; Carollo et al. 1995). These optical studies are confined to within one or two effective radii R_e , and typically find that luminous matter dominates the mass distribution inside $\sim R_e$, while dark matter begins to be dynamically important at $2\text{--}3 R_e$. In particular, for a sample of X-ray emitting galaxies, it has been found that dark matter halos are not much more massive than the luminous component, with the dark-to-luminous mass ratio $M_h/M_* \approx 1 - 6$; the value of $M_h/M_* \sim 2$ is most common (Saglia et al. 1993). X-ray emission from hot gas provides a great potential for mapping the mass of ellipticals to larger distances (e.g., Fabian et al. 1986). The standard method employed derives from the equation of hydrostatic equilibrium, and requires the knowledge of the gas temperature profile. Attempts to apply this technique to the *Einstein* data yielded a much larger component of dark matter than found from optical data, but these results are very uncertain because temperature profiles are poorly determined (Forman, Jones, & Tucker 1985; Fabbiano 1989). Using superior X-ray data provided by *ROSAT* and *ASCA*, Buote & Canizares (1997) proved that mass does not follow the optical light, out to many R_e , in NGC720 and NGC1332. Adopting plausible gas and mass models, they find $M_h/M_* > 3$ for NGC1332, and $M_h/M_* > 7$ in NGC720 at 90% confidence; M_h prevails exterior to R_e . Similarly Mushotzky et al. (1994) derive $M_h/M_* \sim 8$ within $8R_e$ for NGC4636, and analogous results have been obtained from *ROSAT* data of NGC507 and NGC499 by Kim & Fabbiano (1995). *AXAF* will have the combined spatial and spectral resolution to measure accurately the presence of different spectral components, their relative flux and their spatial distribution, and to produce more accurate mass distribution from X-rays.

The radial density distribution of the dark haloes of ellipticals is not well constrained by observations; theo-

retical arguments favor a peaked profile (Ciotti & Pellegrini 1992; Evans & Collett 1997), and high resolution numerical simulations of dissipationless collapse produce a density distribution with $\gamma \simeq 1$ near the center (Dubinski & Carlberg 1991; Navarro, Frenk, & White 1996; White 1996; Fukushige & Makino 1997, and references therein). Previous works studying the hot gas flow evolution always used quasi isothermal haloes at least nine times more massive than the luminous component. We are motivated now to explore even the effects produced by dark haloes not as massive as supposed before, and not quasi-isothermal.

1.3. New Type Ia supernova rates

Nearby SNIa rates in early-type galaxies have been carefully reanalyzed recently, and this important ingredient of the simulations of hot gas flows has been revised. From optical surveys it was estimated to be $0.88 h^2$ SNU (Tammann 1982), and then $0.98 h^2$ SNU (van den Bergh & Tammann 1991). Most recent estimates agree on lower values: $0.25 h^2$ SNU (van den Bergh & McClure 1994) and $0.24 h^2$ SNU (Turatto, Cappellaro, & Benetti 1994), where $h = H_0/100$ and $1 \text{ SNU} = 1 \text{ SNIa per century per } 10^{10} L_{B\odot}$.

In principle, constraints on the SNIa rate can be given also by estimates of the iron abundance in galactic flows (see, e.g., Renzini et al. 1993, and references therein). These were first attempted using data from the *Ginga* satellite for NGC4472, NGC4636, NGC1399 (Ohashi et al. 1990; Awaki et al. 1991; Ikebe et al. 1992), and then from the *BBXRT* satellite for NGC1399, NGC4472 (Serlemitsos et al. 1993), and more recently from *ASCA* with a superior spectral energy resolution (Loewenstein et al. 1994; Awaki et al. 1994; Arimoto et al. 1997; Matsumoto et al. 1997). Under the assumption of solar abundance ratio, the analysis of all these data suggests a very low iron abundance, consistent with no SNIa's enrichment and even lower than that of the stellar component. However, some authors have found that more complex multi-temperature models with higher abundance give a better fit of the data (Kim et al. 1996, Buote & Fabian 1997). Moreover, the above results are based on iron line diagnostic tools whose reliability has been questioned (e.g., Arimoto et al. 1997), especially because of uncertainties affecting the Fe L-shell atomic physics for temperatures less than 2 keV, that are typical of hot gas flows in ellipticals (Liedahl, Osterheld, & Goldstein 1995). Line emission even in simple (e.g., isothermal) astrophysical plasmas needs to be understood, and reliable fits to the data made, before secure consequences concerning the SNIa rate can be drawn from X-ray determined abundances.

In summary, recent optical studies agree on a present epoch SNIa rate much lower than previously used, and indicate that also the dark matter content could be lower.

Moreover, cuspier density profiles, especially for the stellar distribution, should be used. All this raises the question of whether the C DPR scenario is altered by these changes in the main ingredients of the problem, and more in general what are the effects on the properties of hot gas flows. In this paper we address these points, with a new set of hydrodynamical simulations. In Section 2 we present the galaxy models, the source terms, and the integration techniques. In Section 3 we discuss the main properties of the evolution of gas flows in our new models, and we compare them with the observations and the C DPR results. In Section 4 we discuss the results using energetic arguments, and in Section 5 the main conclusions are summarized.

2. The models

2.1. Galaxy models

Following the discussion in Sections 1.1 and 1.2, our model galaxies are a superposition of a Jaffe density distribution for the luminous matter ρ_* [eq. (1) with $M = M_*$, $r_c = r_*$, $\gamma = 2$], and of a Hernquist distribution for the dark matter [eq. (1) with $M = M_h$, $r_c = r_h$, $\gamma = 1$]. We call these two-component mass models JH models. Both density distributions have finite mass, and so no truncation radius is applied. The relation between the scale length r_* and the effective radius for the Jaffe model is $R_e \simeq 0.76r_*$. We constrain the luminous body to lie on the fundamental plane of elliptical galaxies (Djorgovski & Davis 1987; Bender, Burstein, & Faber 1992). The input observables are L_B , and the central value of the projected velocity dispersion σ_c . The stellar mass is related to σ_c through the projected virial theorem, as described in Ciotti, Lanzoni, & Renzini (1996); the luminous matter distribution is then completely defined, because it is assumed that the stellar mass-to-light ratio is constant with radius, and the orbital distribution is isotropic. The dark matter distribution is determined by choosing the ratios of the dark to luminous mass ($\mathcal{R} = M_h/M_*$), and of the dark to luminous core radius ($\beta = r_h/r_*$). The basic dynamical properties of the JH models (radial trend of the velocity dispersion, kinetic and potential energy, etc.) are given in the Appendix.

2.2. Source terms

The time evolving input ingredients of the numerical simulations are the rates of stellar mass loss, of SNIa heating, and of thermalization of the stellar velocity dispersion; these are calculated as in C DPR, where a detailed description is given. Here we summarize only the main properties of the input quantities. The stellar mass loss rate is accurately described by $\dot{M}_*(t) \simeq 1.5 \times 10^{-11} L_B t_{15}^{-1.36} M_\odot \text{yr}^{-1}$, where L_B is in L_\odot , and t_{15} is time in units of 15 Gyr; in the numerical code the exact mass return prescribed by the stellar evolution theory is used. The SNIa heating rate is parameterized as $L_{\text{SN}}(t) = E_{\text{SN}} R_{\text{SN}}(t) L_B = 7.1 \times 10^{30} \vartheta_{\text{SN}} L_B t_{15}^{-1.5} \text{erg s}^{-1}$, where

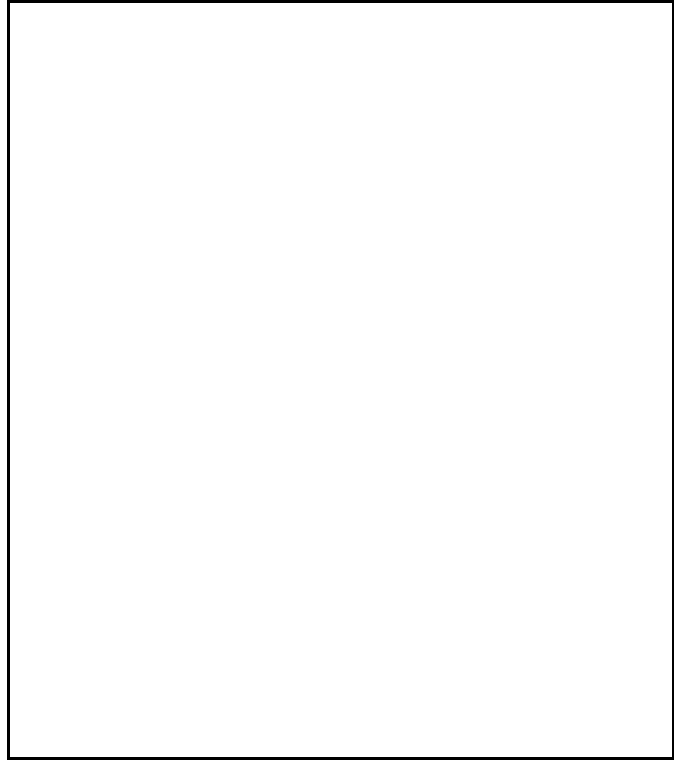


Fig. 2. The cumulative mass profiles normalized to the total stellar mass M_* of JH models with $\mathcal{R} = 2$ and $\mathcal{R} = 9$; the cases $\beta = 2$ and $\beta = 4$ are shown in each panel. Within $r = 2R_e$, $\mathcal{R} = 0.6$ and 0.3 respectively if $\beta = 2$ and $\beta = 4$ (upper panel); $\mathcal{R} = 2.8$ and 1.1 if $\beta = 2$ and $\beta = 4$ (lower panel).

$E_{\text{SN}} = 10^{51} \text{erg}$ is the kinetic energy injected in the ISM by one SNIa, $R_{\text{SN}}(t) = \vartheta_{\text{SN}} 0.88 h^2 t_{15}^{-1.5} \text{SNI}$, and $h = 0.5$. When $\vartheta_{\text{SN}} = 1$ and $t_{15} = 1$ R_{SN} is the rate estimated by Tammann (1982). L_{SN} is assumed to be decreasing with time just faster than the stellar mass loss rate. Unfortunately, given our enduring ignorance of the nature of the SNIa's progenitors (e.g., Branch et al. 1995) the evolution of the SNIa rate is not known; some arguments though, as an observed pronounced correlation of the rate with the star formation rate along the Hubble sequence, favour a declining rate (see also Renzini et al. 1993; Ruiz-Lapuente, Burkert, & Canal 1995; Renzini 1996). With the assumptions above the specific heating for the gas is decreasing with time, and so we have the wind/outflow/inflow secular evolution in the C DPR models (§1). This direction of the evolution of the flow is maintained as long as R_{SN} decreases faster than \dot{M}_* , and the results do not qualitatively depend on the particular slope adopted for R_{SN} ; when this slope is much higher than that of \dot{M}_* , though, too much iron is produced at early times (see Renzini et al. 1993 for a more extensive discussion).

The heating given by the thermalization of the stellar velocity dispersion at each radius is determined using the

velocity dispersion profile obtained by solving the Jeans equation in the global isotropic case (see the Appendix).

2.3. Numerical simulations

The time-dependent equations of hydrodynamics with source terms, and the numerical code used to solve them, are fully described in CDPR, together with the initial conditions. We adopt here a higher spatial resolution in the central regions of the galaxies: the central grid spacing is 30 pc instead of 100 pc. This allows a better sampling of the inner regions now described by a power law, and is adequate to highlight the differences in the flow properties between JH models and King models plus a quasi isothermal dark halo. The model galaxies are initially devoid of gas, a situation produced by the galactic winds established by type II supernovae, early in the evolution of elliptical galaxies. The gas flow evolution is followed for 15 Gyrs.

3. Evolution of the gas flows

We present here the results of the hydrodynamical simulations. The basic input parameters and output quantities are shown in Table 1. Two representative blue luminosities have been used to investigate the typical gas flow behavior, $L_B = 5 \times 10^{10} L_\odot$, and $L_B = 10^{11} L_\odot$; the corresponding M_* are $1.9 \times 10^{11} M_\odot$ and $4.2 \times 10^{11} M_\odot$. Various values of $(\mathcal{R}, \beta, \vartheta_{\text{SN}})$ are chosen. $\vartheta_{\text{SN}} = 0.25$ is close to the most secure current estimate coming from optical surveys (which is $\vartheta_{\text{SN}} \sim 0.27$, see §1.3); to consider the indications coming from the low iron abundances given by X-ray data (§1.2), we also explore the case $\vartheta_{\text{SN}} = 0.1$; for comparison with the long-lived inflow case, we also use $\vartheta_{\text{SN}} = 0$. The distribution of the dark mass is broader than that of the luminous mass ($\beta = 2$ or $\beta = 4$); the dark mass prevails outside one or two R_e if $\mathcal{R} = 9$, or outside a few R_e if $\mathcal{R} = 2$ (Fig. 2).

A general feature of all the evolutionary sequences, except for those with $\vartheta_{\text{SN}} = 0$, is to develop a *central* inflow at early times, while the outer regions are still outgassing, i.e., a decoupled gas flow (see Fig. 3). The inflow region is bordered by a stagnation radius r_{st} that may range from a small fraction of R_e to many R_e , at the end of the evolution (see Table 1). If r_{st} maintains its position within a few R_e , we call the flow *partial wind* (hereafter PW; see the representative case in Fig. 3 and 4); if it increases considerably to more than $10 R_e$, we call the resulting flow global inflow, even though this is strictly the case only when $\vartheta_{\text{SN}} = 0$. In the PW case, radiative losses suppress an outflow in the inner parts of the galaxy, causing a small inflow region, but a wind can be sustained in the external parts, where the gas density is much lower and the gas is also less tightly bound. The X-ray luminosity of PWs and inflows steadily decreases with time, following the decrease of \dot{M}_* and of the heating. Note that the stagnation points resulting from the simulations are well outside the first grid point, so the flow is properly resolved.

Another general trend in the results is that, at fixed \mathcal{R} , as ϑ_{SN} and/or β decrease, the larger are the inflow region, L_X , the mass accreted to the center \dot{M}_{in} , the mass flowing to the center per unit time \dot{M}_{in} , and the smaller is \dot{M}_{out} , the mass escaping the galaxy per unit time, because the heating is lower and/or the dark mass concentration is higher.

3.1. $L_B = 5 \times 10^{10} L_\odot$ models

For $\mathcal{R} = 2$, and $\vartheta_{\text{SN}} > 0$, these galaxies develop PWs with r_{st} varying from $0.02 R_e$ to $\simeq 3 R_e$. When $\vartheta_{\text{SN}} > 0.25$ a global wind persists until the present time, and so L_X is very low. Even when $\vartheta_{\text{SN}} = 0.25$ the hot gas, in PW, shows such a low L_X that the observed X-ray emission must be largely produced by the stellar sources, whose emission has been estimated to be of the order of $\sim 10^{40} \text{ erg s}^{-1}$ (see Fig. 1). When $\vartheta_{\text{SN}} = 0.1$, the final $L_X \lesssim 5 \times 10^{40} \text{ erg s}^{-1}$,

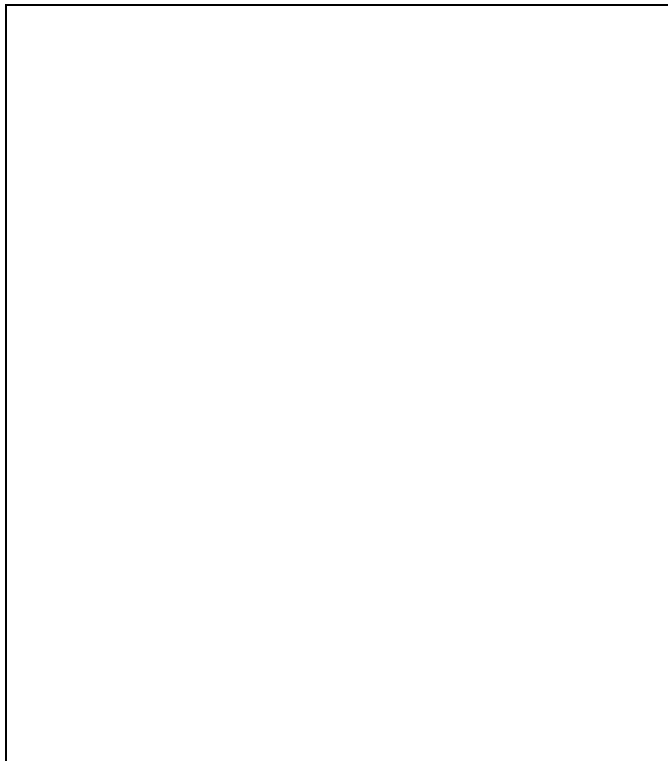


Fig. 3. The evolution of the number density n , the temperature T and the velocity v of the gas, in a typical PW case (the model with $L_B = 10^{11} L_\odot$, $\mathcal{R} = 2$, $\beta = 4$ and $\vartheta_{\text{SN}} = 0.25$ in Table 1). The solid line refers to $t = 1.5$ Gyrs, the dotted line to $t = 4.5$ Gyrs, and the dashed line to $t = 15$ Gyrs. In this model the initially supersonic inflow slows until it becomes fully subsonic at $t \simeq 6$ Gyrs; the outer sonic radius starts at $\sim 2 R_e$ and moves outward, until it establishes at $\sim 8 R_e$ from $t \simeq 10$ Gyrs on.

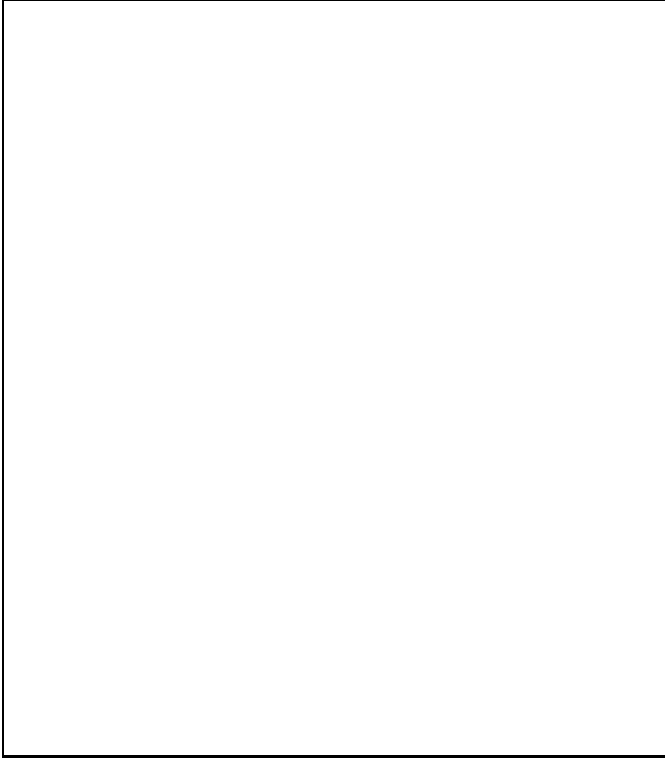


Fig. 4. Upper panel: the time evolution of the mass loss \dot{M}_* , of the mass inflowing into the central sink \dot{M}_{in} , and of the mass lost by the galaxy \dot{M}_{out} . Lower panel: the time evolution of the stagnation radius r_{st} . All refers to the representative model chosen for Fig. 3.

and the hot gas starts to dominate the X-ray emission of the galaxy. Significantly higher L_X values are obtained by increasing the gas temperature, not just by retaining more gas; in fact the model with $\mathcal{R} = 2$ and $\vartheta_{SN} = 0$, a global inflow that lasts for the whole galaxy lifetime, has just $L_X \sim 7 \times 10^{40} \text{ erg s}^{-1}$. To increase the gas temperature *and* L_X , the dark matter content must be increased first, because global winds are obtained by just increasing the SNIa heating. A deeper potential well by itself produces hotter gas, because of a higher gravitational compression during the inflow; moreover, it can be coupled to a larger inflow region, if ϑ_{SN} is kept constant, or to a higher heating without full degassing if ϑ_{SN} is increased.

For $\mathcal{R} = 9$ and $\vartheta_{SN} \lesssim 0.25$ the gas is always in a global inflow at the present time. The highest $L_X \sim 2 \times 10^{41} \text{ erg s}^{-1}$ is obtained when $\vartheta_{SN} = 0.25$ and $\beta = 2$, i.e., when the heating by SNIa's and gravitational compression is the highest possible for the chosen ranges of these parameters. This L_X is still lower than the highest L_X observed at $L_B = 5 \times 10^{10} L_\odot$ (Fig. 1), a problem that was known also from previous works (see the references cited in the Introduction). However, L_X as high as $\sim 10^{42} \text{ erg s}^{-1}$ are comparable to those typical of poor clusters rather than single galaxies; at least

some of them could be explained with accretion effects (see, e.g., Renzini et al. 1993; Bertin & Toniazzo 1995; Kim & Fabbiano 1995).

Note that for PWs ($\mathcal{R} = 2$) L_X is higher when ϑ_{SN} is lower, because the inflow region is larger. For global inflows ($\mathcal{R} = 9$) L_X is higher when ϑ_{SN} is also higher, because the gas is hotter. Altogether, the variation in L_X in Table 1 is a factor of ~ 100 ; it is of a factor of ~ 30 when $\mathcal{R} = 2$, and just ~ 2 when $\mathcal{R} = 9$.

3.2. $L_B = 10^{11} L_\odot$ models

Models with $\mathcal{R} = 2$ again develop PWs, with quite larger central inflow regions than above for the same range of ϑ_{SN} and β values, due to a deeper potential well. The latter makes also the gas hotter. Larger inflow regions and higher gas temperatures, coupled to a larger mass return rate, make the X-ray emission in these galaxies always higher than that of the models described in §3.1, for the same $(\mathcal{R}, \beta, \vartheta_{SN})$. L_X goes from $3 \times 10^{40} \text{ erg s}^{-1}$ to $2 \times 10^{41} \text{ erg s}^{-1}$, when the flow is a PW. So, it is always comparable to or higher than the estimate of the stellar X-ray emission at $L_B = 10^{11} L_\odot$ (Fig. 1); this is in agreement with the fact that in Fig. 1 all galaxies lie above this estimate, for $L_B \gtrsim 10^{11} L_\odot$.

As expected, we always have global inflows if $\mathcal{R} = 9$, and the highest L_X is reached when $\mathcal{R} = 9$ and $\vartheta_{SN} = 0.25$, i.e., again the most efficient way of increasing L_X when the flow is not decoupled is to increase \mathcal{R} , and then ϑ_{SN} . The spread in L_X is of a factor of ~ 10 if $\mathcal{R} = 2$, and very small for global inflows. The total spread is roughly of a factor of 30, lower than for $L_B = 5 \times 10^{10} L_\odot$.

3.3. Other models

In order to investigate how common is the PW phase, we have run two more series of evolutionary sequences corresponding to a low $L_B = 2.2 \times 10^{10} L_\odot$, and to $L_B = 7.1 \times 10^{10} L_\odot$; moreover, also the case $\mathcal{R} = 4$ has been explored. The results are summarized in Table 2. PWs populate again most of the parameter space. The X-ray luminosity of $L_B = 2.2 \times 10^{10} L_\odot$ models remains at low values even at high \mathcal{R} , in agreement with the observations (Fig. 1); for many of these galaxies L_X is likely to be dominated by the stellar emission.

3.4. Emission temperatures and X-ray surface brightness profiles

Emission temperatures of the hot gas have been calculated recently by Matsumoto et al. (1997) and Buote & Fabian (1997), using *ASCA* data and two-temperature model fitting, for about 20 early-type galaxies. These temperatures cover the range $\sim 0.3 - 1.0 \text{ keV}$, and the bulk of values lies within $0.5 - 0.8 \text{ keV}$. The X-ray luminosity weighted emission temperatures of the models are given in Tables 1 and 2. They lie in the range $\sim 0.3 - 0.8 \text{ keV}$, and so are in

Table 1. Results of the JH model evolution. L_X is calculated for the (0.2–4) keV band; T is the emission weighted temperature of the flow. \dot{M}_{in} is the gas mass flow to the center in 15 Gyrs; \dot{M}_{in} and \dot{M}_{out} are the gas masses that flow to the central sink and are lost from the galaxy, per unit time, at 15 Gyrs. At this time $\dot{M}_* = 0.72 M_\odot/\text{yr}$, for the model with $L_B = 5 \times 10^{10} L_\odot$, and $\dot{M}_* = 1.44 M_\odot/\text{yr}$ for the model with $L_B = 10^{11} L_\odot$. χ is defined in §4.

Model	L_B (L_\odot)	\dot{M}_{in} (M_\odot/yr)	\dot{M}_{out} (M_\odot/yr)	\dot{M}_* (M_\odot/yr)	L_X (L_\odot)	T (keV)	χ
1	5×10^{10}	0.72	0.72	0.72
2	10^{11}	1.44	1.44	1.44

good agreement with those observed. They increase with central velocity dispersion, dark matter mass, and SNIa rate. Note how a substantial SNIa’s heating helps obtaining temperatures close to those observed; other possible sources of heating not studied here are the presence of an external pressure due to an intracluster or intragroup medium (e.g., Bertin & Toniazzi 1995), and that of a central black hole (Ciotti & Ostriker 1997).

The comparison with the observed X-ray surface brightness profiles $\Sigma_X(R)$ is more delicate, because there is not a typical profile, nor a range of typical profiles. In the next, first we examine what kind of $\Sigma_X(R)$ are shown by PWs (which are the resulting flow regimes of the bulk of the galaxies, in our scenario), and then we discuss how $\Sigma_X(R)$ of our models compare with the available observations.

In Fig. 5 we compare the *shapes* of the X-ray profiles of partial wind solutions with different stagnation radii with that of a global inflow with $\vartheta_{\text{SN}} = 0$ (which closely resembles the cooling flow solution). When the stagnation radius is larger than the optical effective radius, the shape of $\Sigma_X(R)$ is indistinguishable from that of the inflow, over most of the galaxy. PWs with very small stagnation radii are instead less steep outside $\sim R_e$; this is because in the external regions the gas density is actually lower for the

PW than for the inflow, but the prevailing effect is given by the higher gas temperature of the PW, produced by the higher ϑ_{SN} . So, judging from the shape of the $\Sigma_X(R)$ profile, inflows and PWs should be indistinguishable by X-ray observations, if r_{st} is a few R_e . Of course, when r_{st} is very small, L_X is very low too, and so these PWs are much less detectable by X-ray observations than global inflows.

Now let’s turn to the comparison with the observations. When L_X of the gas flow is very low, and the X-ray emission is dominated by the contribution of the stellar sources, our models exhibit the X-ray profile of the underlying stellar population. No detailed $\Sigma_X(R)$ for low L_X/L_B galaxies is available yet from the observations. When L_X of the flow is high, the observations – especially those produced by *ROSAT* – show a large variety of shapes for $\Sigma_X(R)$, often modified also by the interaction with the environment (e.g., Trinchieri, Fabbiano & Kim 1997). Using *Einstein* data, Trinchieri, Fabbiano, & Canizares (1986) found that the observed $\Sigma_X(R)$ tend to follow the optical ones, for few best studied X-ray bright galaxies. In our scenario such galaxies host PWs with large stagnation radii, or inflows; these flow phases have the same problems as cooling flows to reproduce X-ray profiles following the optical ones: they are too peaked (see

Table 2. Results of additional JH model evolutions. All quantities are defined as in Table 1. After 15 Gyrs $\dot{M}_* = 0.32 M_\odot/\text{yr}$, for the model with $L_B = 2.2 \times 10^{10} L_\odot$, and $\dot{M}_* = 1.02 M_\odot/\text{yr}$ for the model with $L_B = 7.1 \times 10^{10} L_\odot$. At fixed L_B , the models with the larger R_e are less concentrated than required for them to lay exactly on the fundamental plane.

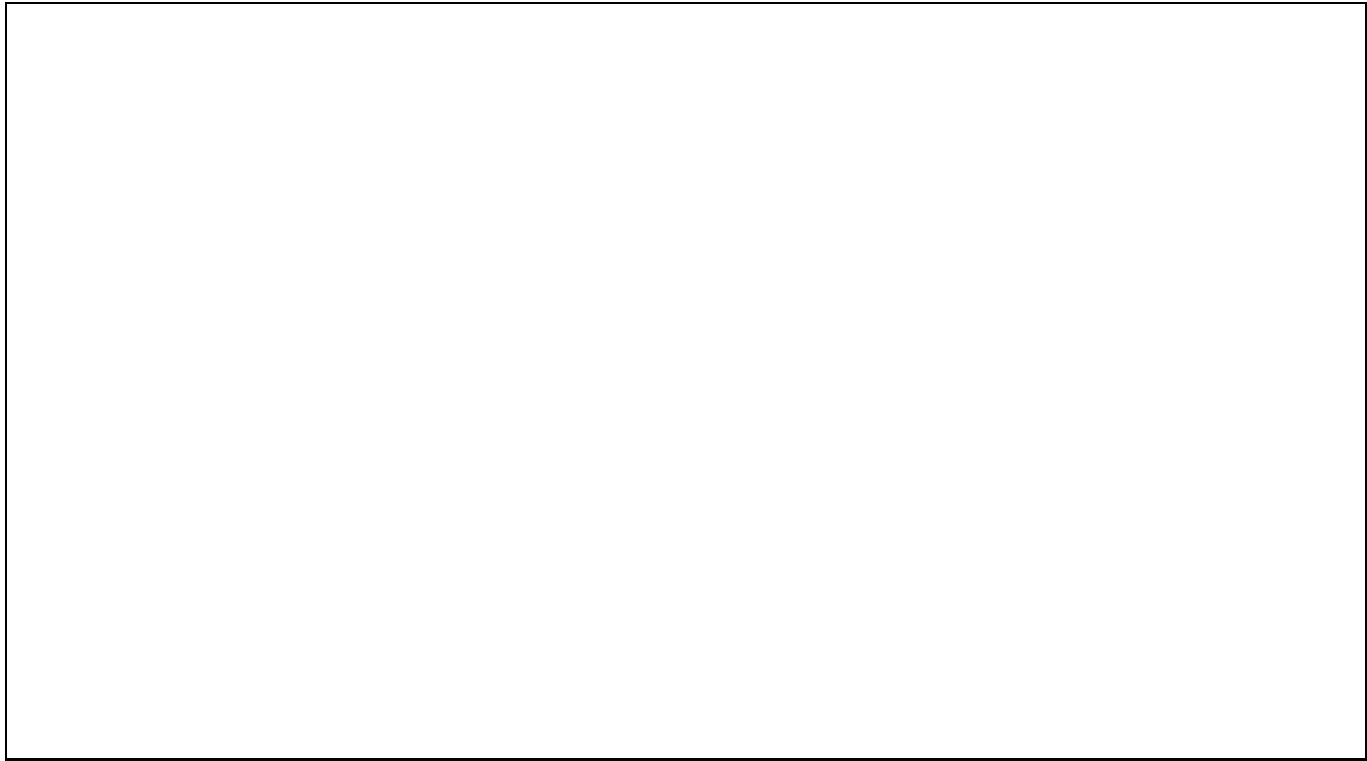


Fig. 5). They can be brought in agreement with the observed $\Sigma_X(R)$ by the introduction of distributed mass deposition due to thermal instabilities in the hot gas, as shown and discussed in detail by Sarazin & Ashe 1989, and Bertin & Toniazzo 1995; another possibility is stationary convective accretion onto a central massive black hole (Tabor & Binney 1993), or unstable accretion (Ciotti & Ostriker 1997).

A detailed comparison with $\Sigma_X(R)$ observed for a specific galaxy requires a large number of simulations to find whether there is a combination of input parameters (with the possible addition of the effect of the environment, and/or of a central black hole) that gives a model reproducing the observations. This goes beyond the scope of this paper; it has been done successfully for NGC4365, in the framework of the CDPR scenario, by Pellegrini & Fabbiano (1994).

3.5. Effects of the new ingredients

We summarize here the main properties of the flows, and the main differences with the results obtained by CDPR, produced by the new mass distributions and by the reduction of ϑ_{SN} and \mathcal{R} . The global wind phase disappears for all galaxies except the smallest ones (see the case $L_B = 2.2 \times 10^{10} L_\odot$ in Table 2): a central inflow, even though very small, is always present from the beginning

of the evolution. As a consequence the outflow phase – the transition from a global wind to a global inflow in CDPR – also disappears. Large L_X variations are produced in the JH models by the different size of the central inflow region. Most of the observed spread in L_X at fixed L_B can be reproduced again, as it was in CDPR (Fig. 1): besides the observed variation from galaxy to galaxy in σ_c and in the concentration R_e , a spread in the dark matter content, and/or a variation in the SNIa rate can produce large variations in r_{st} and in the gas temperature, and then in L_X (of even a factor of ~ 100 , Table 1 and Fig. 1). If \mathcal{R} remains at low values ($\mathcal{R} \lesssim 4$), though, it is difficult to reproduce L_X higher than a few times $10^{41} \text{ erg s}^{-1}$ (Table 2), and so to cover all the observed L_X variation. Moreover, for a given range of variation of \mathcal{R} and ϑ_{SN} , more luminous galaxies show less scatter in L_X .

Another property of the flows in JH models is to accumulate cold gas at their centers, during the evolution (M_{in} in Tables 1 and 2). This mass when $\vartheta_{\text{SN}} > 0$ ranges from $10^9 M_\odot$ to $2 \times 10^{11} M_\odot$. Evidence of cold gas at the center of bright X-ray galaxies has come recently from the high column densities (N_H) required to obtain good fits of their X-ray spectra. The *BBXRT* data require $\sim 10^{10} M_\odot$ of cold gas in NGC1399 (Serlemitsos et al. 1993); to fit the *ASCA* data of NGC4472, $3 \times 10^{10} M_\odot$ of cold material are needed (Awaki et al. 1994); *ASCA* data require cen-

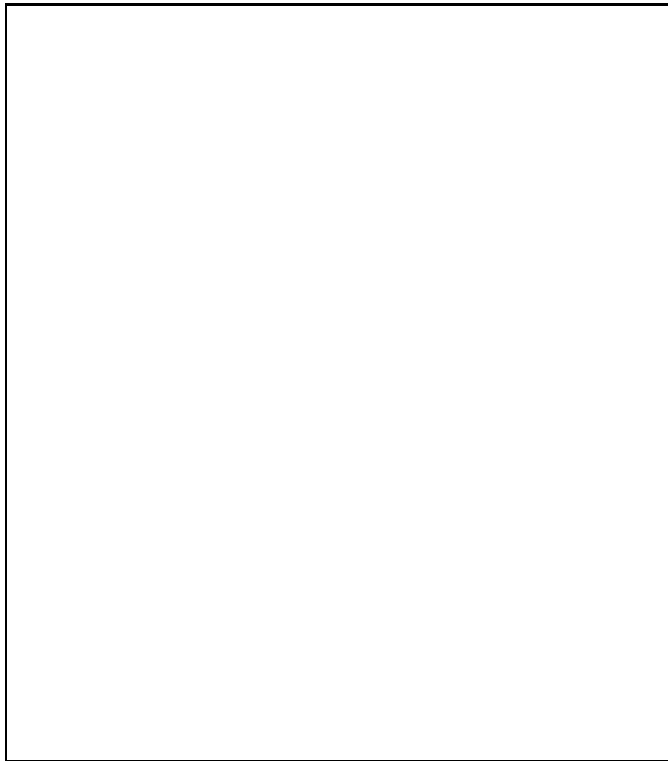


Fig. 5. The X-ray surface brightness profile of three models with $L_B = 5 \times 10^{10} L_\odot$, $\mathcal{R} = 2$ and $\beta = 2$: the solid line corresponds to a global inflow ($\vartheta_{\text{SN}} = 0$), the dotted line to a PW with $r_{\text{st}} = 3.5R_e$ (the model with $\vartheta_{\text{SN}} = 0.1$ in Table 1), and the dashed line to a PW with $r_{\text{st}} = 0.04R_e$ (the model with $\vartheta_{\text{SN}} = 0.25$ in Table 1). The heavy dot-dashed line is the optical surface brightness profile in arbitrary units.

tral column densities larger than the Galactic value also for NGC4636, NGC4406, NGC720, NGC1399, NGC1404, NGC4374 (Arimoto et al. 1997). It has been suggested to explain this finding as the accumulation of cold material by a steady state cooling flow. This accumulation could have been produced by a PW as well; moreover, even different amounts of cold material can be naturally explained in this scenario (see the large variations of M_{in} in Table 1). So, the finding of cold matter at the center of early-type galaxies cannot be considered as evidence for a long lived cooling flow. Note however that the accuracy of these N_H absorption measurements could be affected by the uncertainties plaguing plasma spectra, and producing the iron-L problem (§1.3).

4. An energetic explanation for the occurrence of the PW in different galaxy models

The origin of PWs, and of the flows of a different nature obtained by CDPR, can be explained qualitatively in terms of the *local* χ_ℓ function. The *global* χ is defined as the ratio between the energy required to steadily extract the gas lost by the stars per unit time from the galactic

potential well (L_g), and the heating supplied by the SNIa explosions plus the thermalization of the stellar velocity dispersion (L_σ). χ was introduced by CDPR to predict the expected flow phases in King galaxies, and was shown to work remarkably well by the numerical simulations: when $\chi > 1$ the flow turned out to be an inflow, when $\chi < 1$ a wind. In Tables 1 and 2 most of the resulting flow phases are not global, but PWs, and so we are moved to investigate in more detail the distribution of the energetics inside the galaxy models. This distribution in fact can be much different for two galaxies with the same global χ . The local χ_ℓ is defined as

$$\chi_\ell(r) \equiv \frac{dL_g(r)}{dL_\sigma(r) + dL_{\text{SN}}(r)}, \quad (2)$$

where

$$dL_g(r) = 4\pi\alpha(t)\rho_*(r)|\phi_T(r)|r^2 dr, \quad (3)$$

$$dL_\sigma(r) = 6\pi\alpha(t)\rho_*(r)\sigma_*^2(r)r^2 dr, \quad (4)$$

and

$$dL_{\text{SN}}(r) = \frac{L_{\text{SN}}(t)}{M_*} 4\pi\rho_*(r)r^2 dr, \quad (5)$$

where $\phi_T = \phi_* + \phi_h$ is the total potential, σ_* is the one-dimensional isotropic velocity dispersion obtained by solving the Jeans equations for the adopted mass model (e.g., Binney & Tremaine 1987), and $\alpha(t) = \dot{M}_*/M_*$ is the specific mass return rate. The global χ is obtained by replacing the differentials in equation (2) with their integrals over the whole galaxy.

The differences in the flow behavior of JH models and models with a central constant density region can be understood with the aid of Fig. 6, where χ_ℓ is shown for four representative one-component models. These have the same global χ , and so from an energetical point of view are globally equivalent. Three of them are γ -models, with $\gamma = 2, 1, 0$, i.e., they are the Jaffe model, the Hernquist model, and a model with a core. The fourth density distribution is described in the Appendix, and is flatter at the center than the $\gamma = 0$ model, but for large r it decreases $\propto r^{-4}$, as all the γ -models. This distribution is studied for its similarity with the King (1972) model, that needs the annoying introduction of a truncation radius, and has more complicated dynamical properties.

It is apparent from Fig. 6 that the steeper the density profile, the stronger is the variation of χ_ℓ across the galaxy, and the higher are the values that it reaches at the center. This explains why a strong decoupling can be present in the flow of highly concentrated systems: a χ_ℓ significantly higher than unity in the central regions produces a central inflow, while in the external parts a degassing is energetically possible because $\chi_\ell < 1$. *This can happen when the global χ is either > 1 or < 1* (see Fig. 6 and Table 1), so

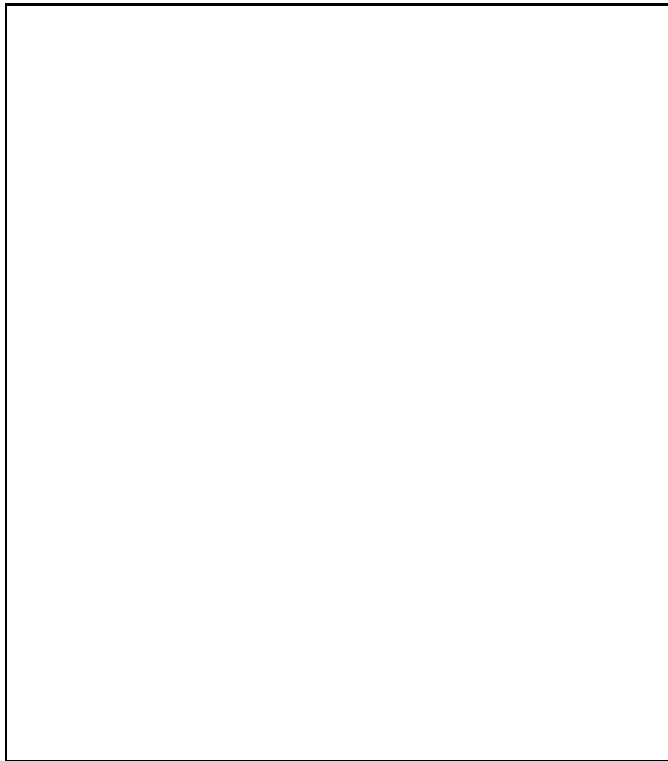


Fig. 6. The radial trend of χ_ℓ as a function of r/R_e for the models considered in §4. The ratio R_e/r_* is given by 0.76, 1.82, 2.87, 1.73 respectively for the Jaffe (solid line), Hernquist (dotted), $\gamma = 0$ (short-dashed) and the model described in the Appendix (long-dashed).

this parameter is not a good indicator of the flow phase for highly concentrated systems. If χ decreases, the radius where $\chi_\ell = 1$ moves inward for all the models, and so a larger part of the galaxy is degassing. Note a fundamental difference in the trend of $\chi_\ell(r)$ as a function of χ for models with a core and cuspy models: while in cuspy models there is always a region with $\chi_\ell > 1$, even though small, this is not the case for core models, in which such a region suddenly appears by increasing χ , with a size larger than the core.

A second effect on χ_ℓ is produced by the dark halo. If this halo is more diffuse than the stellar mass, increasing \mathcal{R} makes more bound the external regions, when χ is kept constant, and so the radius at which $\chi_\ell = 1$ moves outward (see Fig. 7 for the case of JH models).

The trend of $\chi_\ell(r)$ for models with a core explains the results of the numerical simulations for King models plus diffuse quasi-isothermal dark halos obtained by CDPR and Pellegrini & Fabbiano (1994). The flow phases found by CDPR with $\mathcal{R} = 9$ were all global; with low \mathcal{R} , instead, the flow can be decoupled again, as found by Pellegrini & Fabbiano (1994) in their detailed modeling of the X-ray properties of two ellipticals. This because with high \mathcal{R} the region with $\chi_\ell \approx \text{constant}$ is very large (of the

order of the core radius of the dark halo), while with low \mathcal{R} this region is of the order of the stellar core radius.

In summary, the combined effect of SNIa's and dark matter is more varied for models with a core than for JH models: for a large range of \mathcal{R} values, the latter keep in PWs with a varying r_{st} , while the former can be in wind, PWs, outflows or inflows.

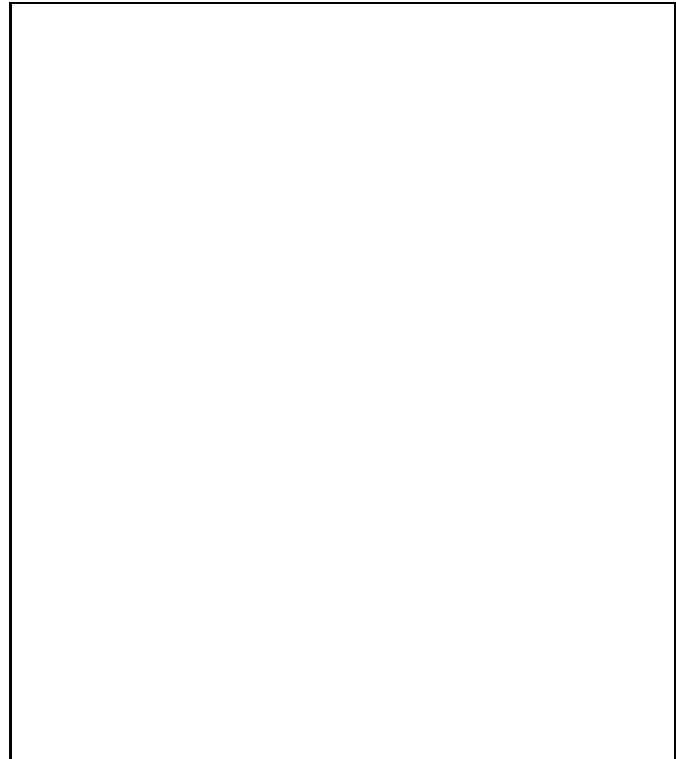


Fig. 7. The radial trend of χ_ℓ as a function of r/R_e for the JH model. The different curves are labelled with the value of \mathcal{R} , while the global χ and β are constant at the values indicated.

5. Conclusions

Using evolutionary hydrodynamical simulations, we have investigated the properties of hot gas flows in elliptical galaxies described by a Jaffe stellar density profile, and containing various amounts of dark matter, distributed as a Hernquist law; the rate of SNIa explosions is one-fourth of the Tammann's rate, or lower. The results can be summarized as follows.

The simulations show that most of the gas flows are strongly decoupled, i.e., they develop an inflow in the central region of the galaxy, while the external parts are still degassing¹. The stagnation radius of these flows (PWs)

¹ Note that decoupled flows are present also in flat and rotating models with low ϑ_{SN} , albeit for reasons different from those causing the PWs studied here (D'Ercole & Ciotti 1997).

may range from a small fraction of the optical effective radius to many R_e . This situation is present even when the global energy balance of the flow indicates that the energy inputs from SNIa's and from the thermalization of the stellar random motions is high enough to unbind all the gas ($\chi < 1$). Alternatively, the gas can be outflowing from the outer part of the galaxy even when the global energy balance indicates that the energy available is less than needed to unbind it all ($\chi > 1$). So, χ is not a good indicator of the flow phase; larger χ values, though, correspond to larger stagnation radii, for a fixed L_B . Global inflows are produced when the dark matter content is so high to bind the gas over the whole galaxy.

The X-ray luminosity of PWs is higher when ϑ_{SN} is lower, because the inflow region is larger; for global inflows L_X is higher when ϑ_{SN} is also higher, because the gas is hotter. The key factor causing large L_X variations in JH models is the size of the central inflow region. The lowest L_X/L_B values observed can be easily reproduced by PWs; high dark matter contents are required to approach the highest L_X observed.

The shape of the X-ray surface brightness profile of PWs is close to that of global inflows, over most of the optical image, if the stagnation radius is a few R_e ; it is externally less peaked than that, if r_{st} is a fraction of R_e , i.e., when the gas is hotter than in the inflow case.

The strong decoupling of the flow is explained by the radial trend of the local energy balance χ_ℓ , that is very peaked for steep mass density profiles as in the JH models. Previously used density profiles which were flat at the center – such as the King models plus quasi-isothermal dark halos – showed a larger tendency to have global flow phases, because also their $\chi_\ell(r)$ is flatter. So, the change of the mass profile has an important effect: both numerical simulations and analytical calculations show how peaked density profiles preferentially develop decoupled gas flows (in the sense that the region of the parameter space populated by PWs is large compared to that of inflows or winds).

The results of our simulations compare with the observations in two main aspects. The first is that most of the observed spread in L_X shown by the data is easily reproduced: the highest L_X are again, as in CDPR, associated with global inflows, while the bulk of the galaxies are now in PW, rather than in outflow; global winds are present only in the smallest galaxies.

The second is that the presence of cold gas at the center of Es, and a peaked X-ray surface brightness profile, cannot be unequivocally associated to a cooling flow: a PW could be present as well, with a significant part of the galaxy degassing. Particularly, a galaxy can have $\vartheta_{\text{SN}} = 0.25$ and still a non negligible amount of cold matter at the center. In addition, since r_{st} varies over a wide range of radii, PWs can accumulate largely varying quantities of cold gas.

Acknowledgements. We wish to thank James Binney, Annibale D'Ercole, Paul Goudfrooij and Alvio Renzini for stimulating discussions. This work has been partially supported by the contract ASI-95-RS-152.

6. Appendix

6.1. The JH models

We derive here the main properties of the JH models that have been used in the numerical simulations and in the computations of χ and χ_ℓ . The reported quantities are dimensionless, and the normalization constants are expressed in terms of the total stellar mass M_* , the core radius r_* and the gravitational constant G ; again $\mathcal{R} = M_h/M_*$ and $\beta = r_h/r_*$. The cumulative mass inside $s = r/r_*$ and the total potential are given by:

$$\tilde{M}(s) = \frac{s}{1+s} + \frac{\mathcal{R}s^2}{(\beta+s)^2}, \quad (6)$$

$$\tilde{\phi}_T(s) = -\ln\left(\frac{1+s}{s}\right) - \frac{\mathcal{R}}{\beta+s}. \quad (7)$$

In the hydrodynamical simulations we used the globally isotropic stellar velocity dispersion profile, that we calculate here. For any two-component model the velocity dispersion profile is given by $\rho_*\sigma_*^2 = I_{**}(s) + \mathcal{R}I_{*h}(s)$, where σ_* is the 1-dimensional radial velocity dispersion. The first term is the isotropic velocity dispersion for the Jaffe model:

$$\tilde{I}_{**}(s) = \frac{(6s^2 + 6s - 1)(2s + 1)}{8\pi s^2(1+s)^2} + \frac{3}{2\pi} \ln \frac{1+s}{s}, \quad (8)$$

and the second one describes the contribution due to the Hernquist dark halo:

$$\tilde{I}_{*h}(s) = \frac{\ln(s)(\beta+1)}{2\pi\beta^3} - \frac{\ln(1+s)(\beta-2)}{2\pi(\beta-1)^3} - \frac{\ln(\beta+s)(2\beta-1)}{2\pi\beta^3(\beta-1)^3} + \frac{2(\beta^2 - \beta + 1)s^2 + (\beta+1)(2\beta^2 - 3\beta + 2)s + \beta(\beta-1)^2}{4\pi\beta^2(\beta+s)(1+s)} \quad (9)$$

Physically acceptable limits can be easily found for $\beta = 0$ (thus mimicking a black hole at the center of a Jaffe model) and for $\beta = 1$.

The cumulative potential and kinetic energies inside r can be found analytically for this two-component model, but for simplicity we report here only their total values. The total potential energy is given by $U_* = U_{**} + \mathcal{R}U_{*h}$, where

$$\tilde{U}_{**} = -\frac{1}{2}, \quad (10)$$

and

$$\tilde{U}_{*h} = -\frac{\beta-1-\ln(\beta)}{(\beta-1)^2}. \quad (11)$$

By integrating over the whole galaxy equation (3), we have $L_g = \alpha(t)(GM_*^2/r_*)(2|\tilde{U}_{**}| + \mathcal{R}|\tilde{U}_{*h}|)$. The kinetic energy is again the sum of two different contributions, $K_* = K_{**} + \mathcal{R}K_{*h}$, where

$$\tilde{K}_{**} = \frac{1}{4}, \quad (12)$$

and

$$\tilde{K}_{*h} = \frac{(\beta + 1) \ln(\beta) + 2(1 - \beta)}{2(\beta - 1)^3}. \quad (13)$$

The integration over the whole galaxy of equation (4) gives $L_\sigma = \alpha(t)(GM_*^2/r_*)(\tilde{K}_{**} + \mathcal{R}\tilde{K}_{*h})$.

6.2. A centrally flat model

Here we derive the dynamical quantities corresponding to the density distribution

$$\tilde{\rho}_*(r) = \frac{1}{\pi^2} \frac{1}{(1 + s^2)^2}. \quad (14)$$

The mass contained inside r is given by

$$\tilde{M}_*(s) = \frac{2}{\pi} \left[\arctan(s) - \frac{s}{1 + s^2} \right], \quad (15)$$

and the potential is

$$\tilde{\phi}_*(s) = -\frac{2}{\pi} \frac{\arctan(s)}{s}. \quad (16)$$

The globally isotropic velocity dispersion is given by:

$$\tilde{I}_{**}(s) = \frac{3 \arctan(s)^2}{2\pi^3} + \frac{(2 + 3s^2) \arctan(s)}{s(1 + s^2)\pi^3} + \frac{4 + 3s^2}{2(1 + s^2)^2\pi^3} \quad (17)$$

As for the JH model, the potential and the kinetic energy inside the radius r can be expressed analytically, but here we give only their total values, being the only ingredient required in the definition of χ :

$$\tilde{U}_{**} = -\frac{1}{2\pi}, \quad (18)$$

and

$$\tilde{K}_{**} = \frac{1}{4\pi}. \quad (19)$$

Finally, the projected distribution associated to $\tilde{\rho}_*$ is:

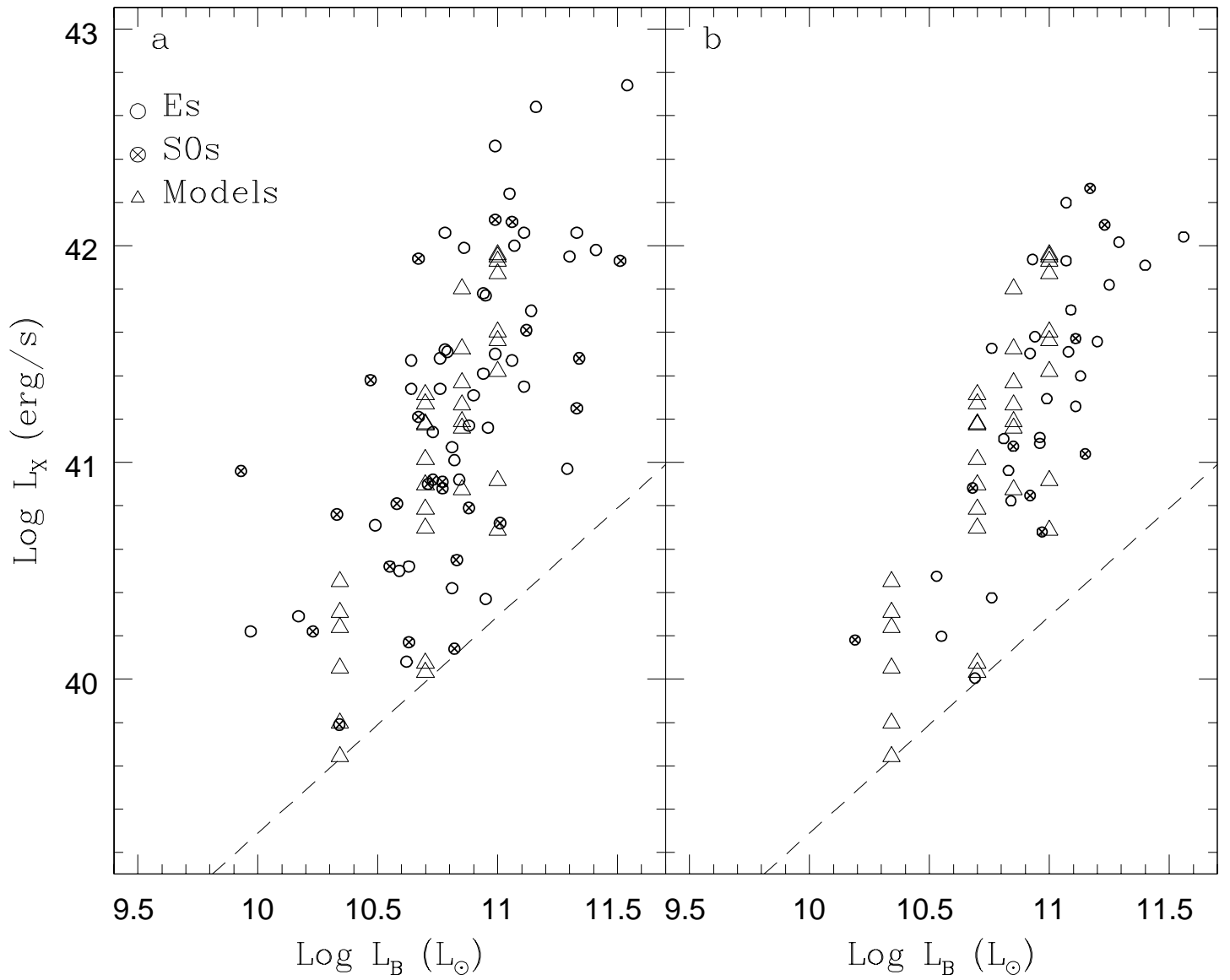
$$\tilde{\Sigma}_*(R) = \frac{1}{2\pi(1 + \tilde{R}^2)^{3/2}}, \quad (20)$$

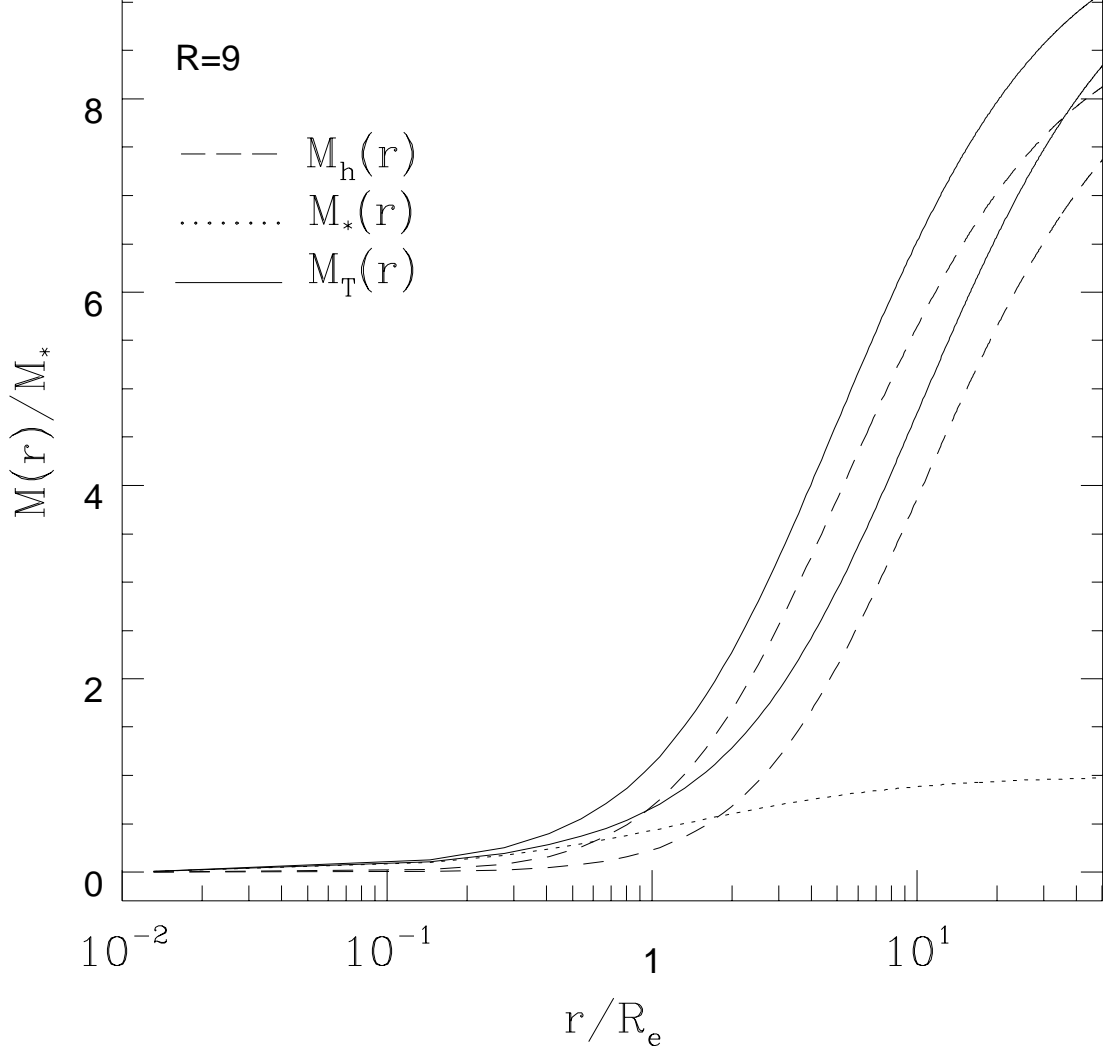
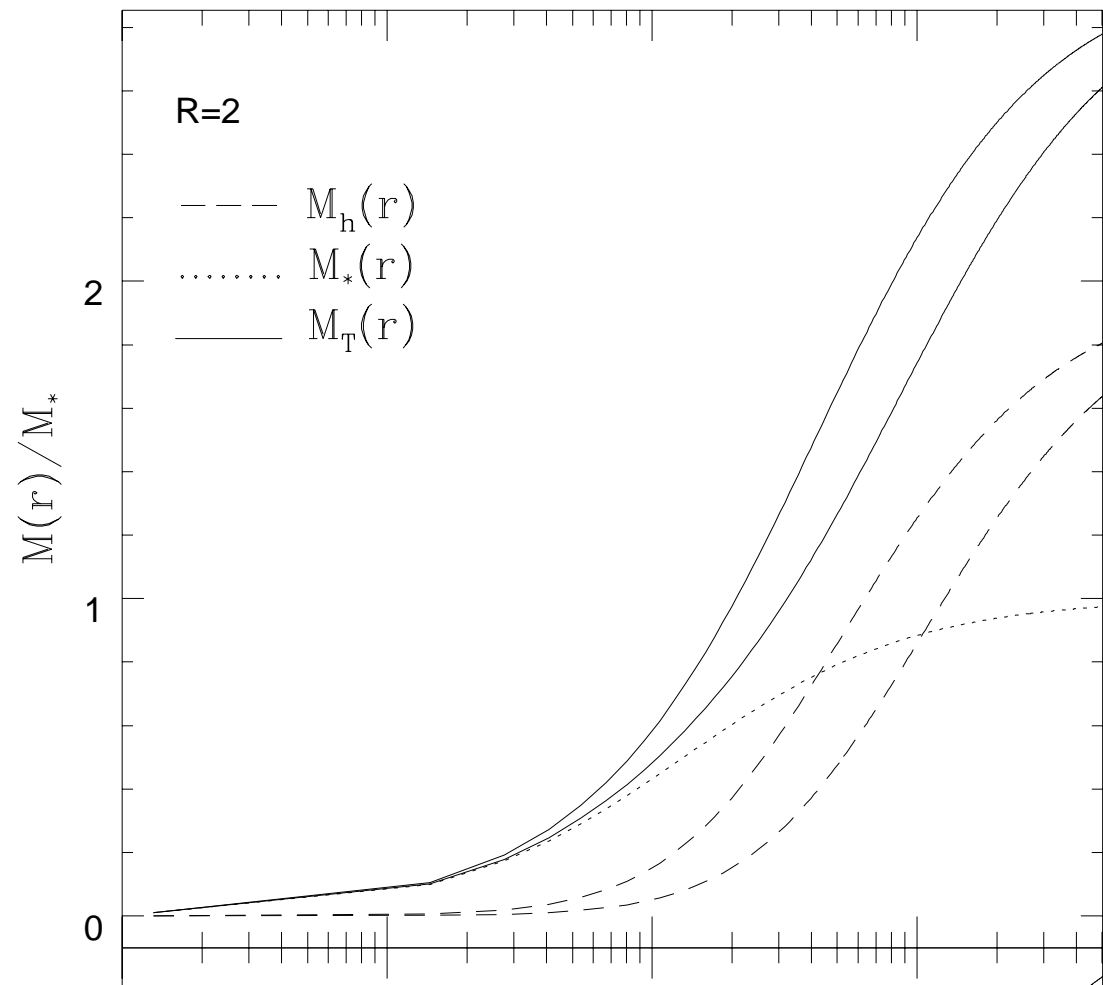
from which one obtains $R_e = \sqrt{3}r_*$.

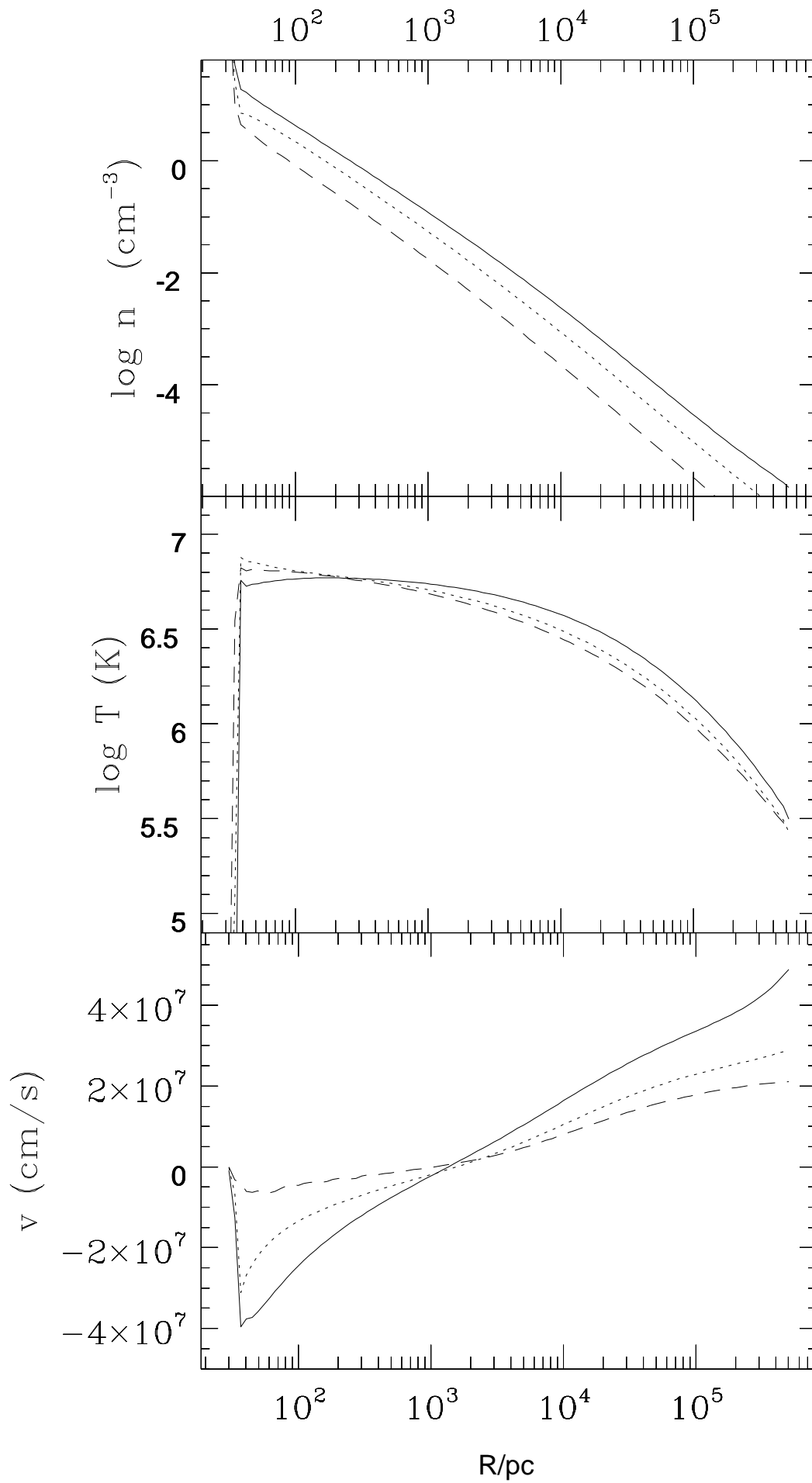
References

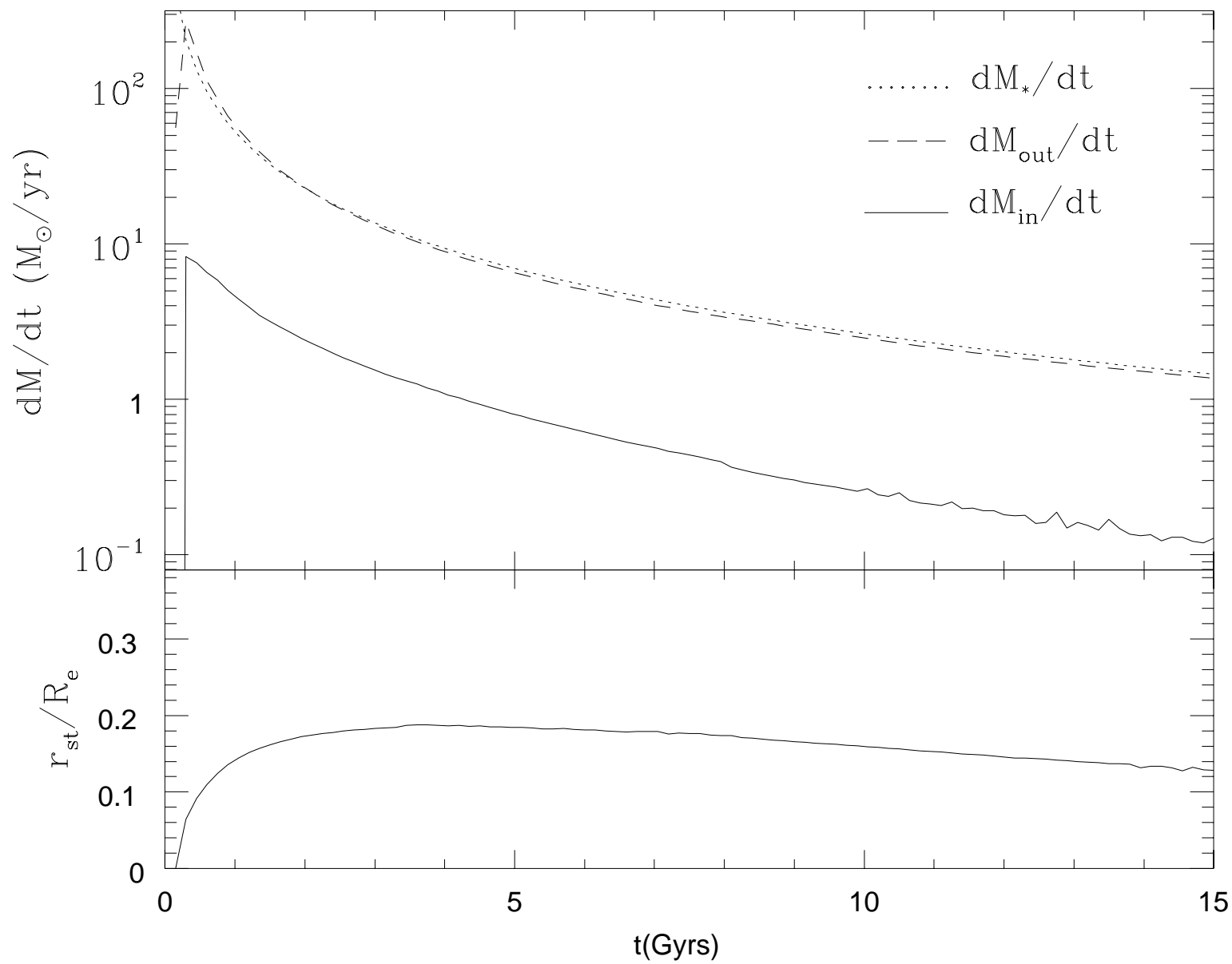
- Arimoto, N., Matsushita, K., Ishimaru, Y., Ohashi, T., & Renzini, A. 1997, ApJ, 477, 128
- Awaki, H., Koyama, K., Kunieda, H., Takano, S., Tawara, Y., & Ohashi, T. 1991, ApJ, 366, 88
- Awaki, H., et al. 1994, PASJ, 46, L65
- Bender, R., Burstein, D., & Faber, S. M. 1992, ApJ, 399, 462
- Bertin, G., Bertola, F., Buson, L. M., Danziger, I. J., Dejonghe, H., Sadler, E. M., Saglia, R. P., de Zeeuw, P. T., & Zeilinger, W. W. 1994, A&A, 292, 381
- Bertin, G., & Toniazio, T. 1995, ApJ, 451, 111
- Binney, J., & Tremaine, S. 1987, Galactic Dynamics, Princeton: Princeton Univ. Press
- Buote, D. A., & Canizares, C.R. 1997, ApJ, 474, 650
- Buote, D.A., & Fabian, A.C., 1997, submitted to MNRAS, (astro-ph/9707117)
- Byun, Y. I., Grillmair, C., Faber, S. M., Ajhar, E. A., Dressler, A., Kormendy, J., Lauer, T. R., Richstone, D. O., & Tremaine, S. D. 1996, AJ, 111, 1889
- Canizares, C.R., Fabbiano, G., & Trinchieri 1987, ApJ, 312, 503
- Carollo, C.M., de Zeeuw, P.T., van der Marel, R.P., Danziger, I.J., & Qian, E.E. 1995, ApJL, 441, L25
- Ciotti, L., D'Ercole, A., Pellegrini, S., & Renzini, A. 1991, ApJ, 376, 380 (CDPR)
- Ciotti, L., & Pellegrini, S. 1992, MNRAS, 255, 561
- Ciotti, L., Lanzoni, B., & Renzini, A. 1996, MNRAS, 282, 1
- Ciotti, L., & Ostriker, J.P. 1997, ApJ, 487, L105
- David, L. P., Forman, W., & Jones, C. 1990, ApJ, 359, 29
- David, L. P., Forman, W., & Jones, C. 1991, ApJ, 369, 121
- Dehnen, W. 1993, MNRAS, 265, 250
- D'Ercole, A., & Ciotti, L. 1997, ApJ, in press
- D'Ercole, A., Renzini, A., Ciotti, L., & Pellegrini, S. 1989, ApJL, 341, L9
- de Vaucouleurs, G. 1948, Ann.Ap., 11, 247
- Djorgovski, S., & Davis, M. 1987, ApJ, 313, 59
- Donnelly, R.H., Faber, S.M., & O'Connell, R.M. 1990, ApJ, 354, 52
- Dubinski, J., & Carlberg, R. G. 1991, ApJ, 378, 496
- Eskridge, P., Fabbiano, G., & Kim, D.W. 1995, ApJ, 442, 523
- Evans, N.W., & Collett, J.L. 1997, ApJL, 480, L103
- Fabbiano, G., 1989, ARAA, 27, 87
- Fabbiano, G., Kim, D. W., & Trinchieri, G. 1992, ApJS, 80, 531
- Fabian, A.C., Thomas, P.A., White, R.E.III, & Fall, S.M. 1986, MNRAS, 221, 1049
- Forman, W., Jones, C., & Tucker, W. 1985, ApJ, 293, 102
- Fukushige, T., & Makino, J. 1997, ApJL, 477, L9
- Hernquist, L. 1990, ApJ, 536, 359
- Ikebe, Y., et al. 1992, ApJ, 384, L5
- Jaffe, W. 1983, MNRAS, 202, 995
- Jaffe, W., Ford, H. C., O'Connell, R. W., van den Bosch, F. C., & Ferrarese, L. 1994, AJ, 108, 1567
- Kim, D. W., Fabbiano, G., & Trinchieri, G. 1992, ApJ, 393, 134
- Kim, D. W., & Fabbiano, G. 1995, ApJ, 441, 182
- Kim, D. W., Fabbiano, G., Matsumoto, H., Koyama, K., & Trinchieri, G. 1996, ApJ, 468, 175
- King, I. 1972, ApJL, 174, L123
- Kormendy, J. 1985, ApJ, 292, L9

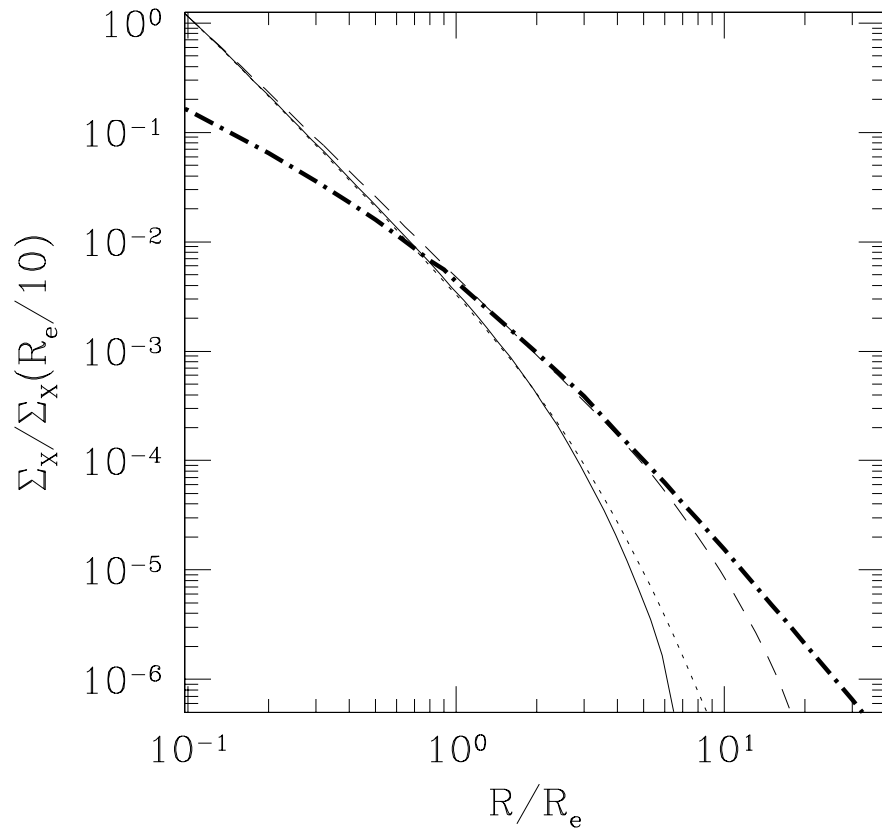
- Lauer, T.R. 1985, *ApJ*, 292, 104
- Lauer, T. R., Ajhar, E. A., Byun, Y. I., Dressler, A., Faber, S. M., Grillmair, C., Kormendy, J., Richstone, D. O., & Tremaine, S. D. 1995, *AJ*, 110, 2622
- Liedahl, D., Osterheld, A., & Goldstein, W. 1995, *ApJ*, 438, L115
- Loewenstein, M., & Mathews, W. G. 1987, *ApJ*, 319, 614
- Loewenstein, M., Mushotzky, R., Tamura, T., Ikebe, Y., Makishima, K., Matsushita, K., Awaki, H., & Serlemitsos, P. J. 1994, *ApJ*, 436, L75
- Mathews, W. G., & Loewenstein M. 1986, *ApJL*, 306, L7
- Matsumoto, H., Koyama, K., Awaki, H., Tsuru, T., Loewenstein, M., Matsushita, K. 1997, *ApJ*, 482, 133
- Møller, P., Stiavelli, M., & Zeilinger, W. W. 1995, *MNRAS*, 276, 979
- Mushotzky, R. F., Loewenstein, M., Awaki, H., Makishima, K., Matsushita, K., & Matsumoto, H. 1994, *ApJ*, 436, L79
- Navarro, J., Frenk, C., & White, S. M. 1996, *ApJ*, 462, 563
- Nulsen, P.E.J., Stewart, G.C., & Fabian, A. C. 1984, *MNRAS*, 208, 185
- Ohashi, T., et al. 1990, in *Windows on Galaxies*, ed. G. Fabbiano, J.A. Gallagher, & A. Renzini (Dordrecht: Kluwer), 243
- Pellegrini, S., & Fabbiano, G. 1994, *ApJ*, 429, 105
- Pizzella, A., Amico, P., Bertola, F., Buson, L.M., Danziger, I.J., Dejonghe, H., Sadler, E.M., Saglia, R.P., de Zeeuw, P.T., & Zeilinger, W.W., 1997, *A&A*, 323, 349
- Renzini, A. 1996, in *Supernovae and Supernova Remnants*, ed. R. McCray, & Z. Wang (Cambridge: Cambridge Univ. Press), 77
- Renzini, A., Ciotti, L., D'Ercole, A., & Pellegrini, S. 1993, *ApJ*, 419, 53
- Ruiz-Lapuente, P., Burkert, A., & Canal, R. 1995, *ApJ*, 447, L69
- Saglia, R. P., et al. 1993, *ApJ*, 403, 567
- Sarazin, C. L., & White, R. E. 1987, *ApJ*, 320, 32
- Sarazin, C. L., & White, R. E. 1988, *ApJ*, 331, 102
- Sarazin, C. L., & Ashe, G. A. 1989, *ApJ*, 345, 22
- Serlemitsos, P. J., Loewenstein, M., Mushotzky, R., Marshall, F., & Petre, R. 1993, *ApJ*, 413, 518
- Tabor, G., & Binney, J. 1993, *MNRAS*, 263, 323
- Tammann, G. A. 1982, in *Supernovae: A Survey of Current Research*, ed. M. Rees, & R. Stoneham (Dordrecht: Reidel), 371
- Tremaine, S. D., Richstone, D. O., Byun, Y. I., Dressler, A., Faber, S. M., Grillmair, C., Kormendy, J., & Lauer, T. R. 1994, *AJ*, 107, 634
- Trinchieri, G., Fabbiano G., & Canizares, C. R. 1986, *ApJ*, 310, 637
- Trinchieri, G., Fabbiano G., & Kim, D.W. 1997, *A&A*, 318, 361
- Turatto, M., Cappellaro, E., & Benetti, S. 1994, *AJ*, 108, 202
- van den Bergh, S., & Tammann G. A., 1991, *ARAA*, 29, 363
- van den Bergh, S., & McClure, R. D. 1994, *ApJ*, 425, 205
- White, S. D. M. 1996, in *Gravitational Dynamics*, Proc. of the 36th Herstmonceux Conference, ed. O. Lahav, E. Terlevich, & R. Terlevich, (Cambridge: Cambridge University Press), in press
- White, R. E., & Sarazin, C. L. 1991, *ApJ*, 367, 476

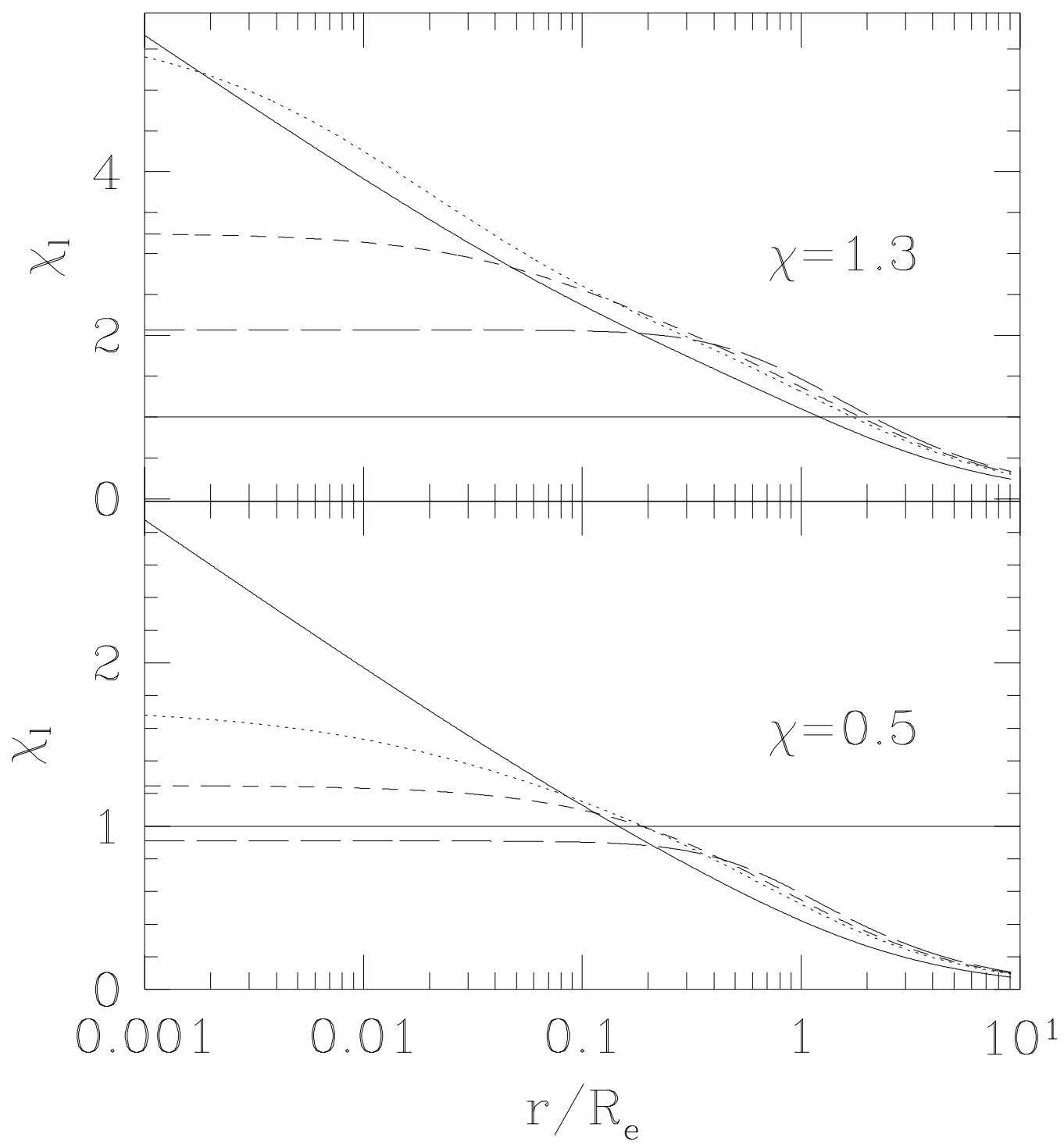


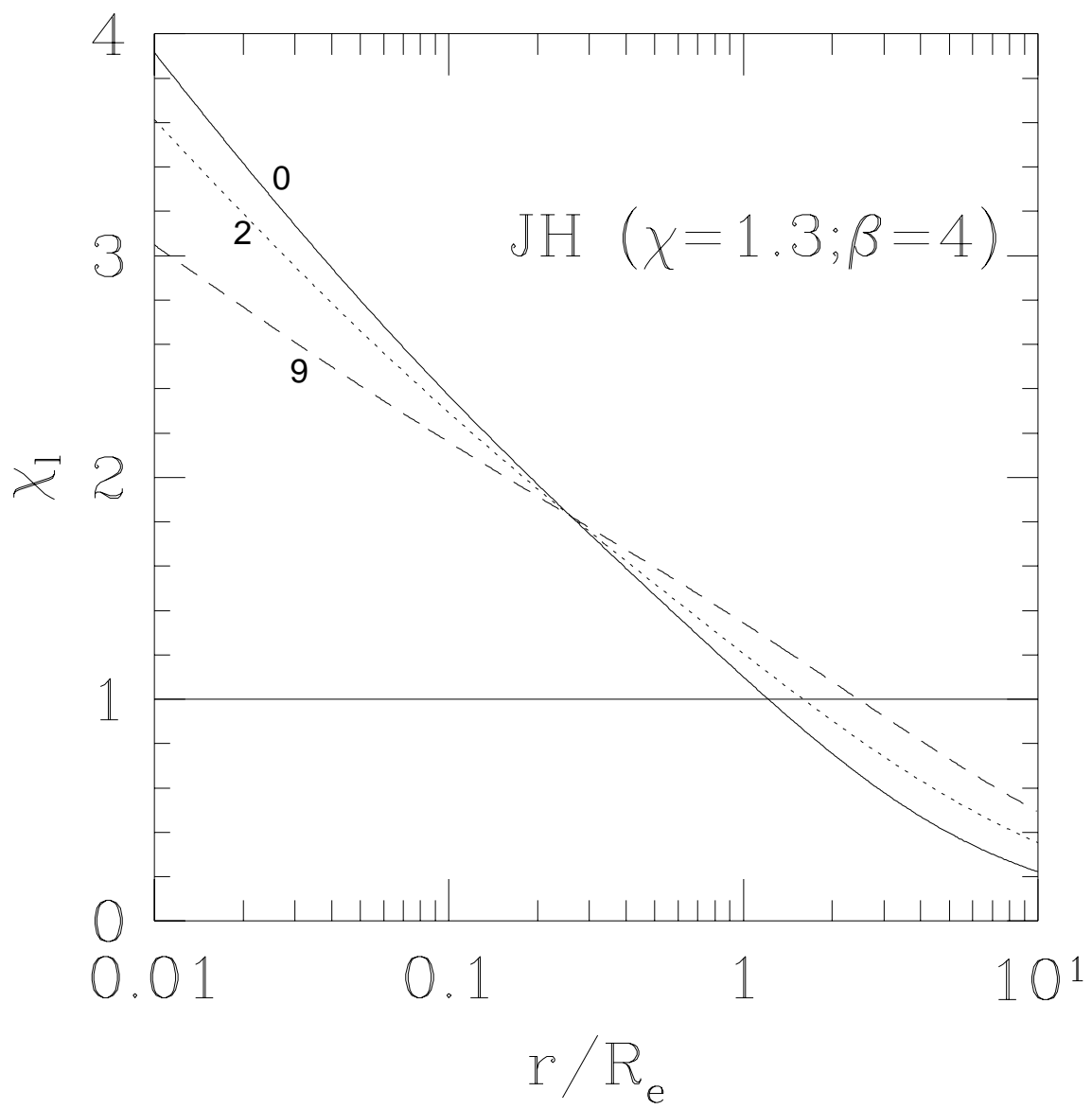












L_B ($10^{10}L_\odot$)	σ_c (km/s)	R_e (pc)	\mathcal{R}	ϑ_{SN}	β	χ	L_X (10^{40}erg/s)	Flow	\dot{M}_{in} ($10^{10}M_\odot$)	\dot{M}_{in} (M_\odot/yr)	\dot{M}_{out} (M_\odot/yr)	r_{st}/R_e	T (keV)			
5	230	5423	2	0.25	2	0.8	0.21	PW	0.27	0.03	0.76	0.04	0.4			
			2	0.25	4	0.7	0.10	PW	0.17	0.01	0.76	0.02	0.4			
			2	0.10	2	1.6	5.12	PW	8.32	0.60	0.24	3.5	0.3			
			2	0.10	4	1.4	4.00	PW	7.76	0.44	0.26	2.0	0.3			
			2	0.00	2	4.0	6.91	I	11.2	0.71	0.00	> 20	0.3			
			9	0.25	2	1.6	19.6	I	5.01	0.83	0.01	> 20	0.5			
			9	0.25	4	1.2	14.1	I	3.39	0.57	0.10	> 10	0.4			
			9	0.10	2	2.9	17.7	I	9.33	0.79	0.00	> 20	0.4			
			9	0.10	4	2.4	9.33	I	9.12	0.74	0.00	> 20	0.3			
			9	0.00	2	6.2	13.9	I	11.2	0.75	0.00	> 20	0.4			
			10	280	8345	2	0.25	2	1.1	6.29	PW	3.16	0.33	1.23	0.40	0.6
						2	0.25	4	0.9	2.93	PW	1.78	0.13	1.36	0.13	0.5
2	0.10	2				2.0	34.6	I	15.9	1.43	0.02	> 10	0.5			
2	0.10	4				1.8	24.4	PW	14.8	1.16	0.14	5.5	0.5			
2	0.00	2				4.9	38.1	I	22.9	1.43	0.00	> 20	0.5			
9	0.25	2				2.1	87.0	I	14.8	1.63	0.00	> 10	0.7			
9	0.25	4				1.6	89.0	I	13.8	2.10	0.00	> 10	0.6			
9	0.10	2				3.5	83.0	I	19.5	1.73	0.00	> 10	0.6			
9	0.00	2				6.2	72.3	I	21.9	1.68	0.00	> 20	0.6			

TAB. 1

L_B ($10^{10}L_\odot$)	σ_c (km/s)	R_e (pc)	\mathcal{R}	ϑ_{SN}	β	χ	L_X (10^{40}erg/s)	Flow	M_{in} ($10^{10}M_\odot$)	\dot{M}_{in} (M_\odot/yr)	\dot{M}_{out} (M_\odot/yr)	r_{st}/R_e	T (keV)		
2.2	210	2715	2	0.25	2	0.7	0.01	W	0.00	0.00	0.35	0.00	0.3		
			4	0.25	2	0.9	0.2	PW	0.10	0.01	0.35	0.08	0.3		
			9	0.25	2	1.4	2.4	PW	1.70	0.20	0.12	2.44	0.4		
		4390	2	0.10	2	1.4	0.7	PW	2.34	0.13	0.29	1.02	0.3		
			2	0.00	2	4.9	1.6	I	4.90	0.29	0.00	> 20	0.3		
			4	0.10	2	1.8	1.3	PW	2.95	0.20	0.23	2.40	0.3		
		7.1	290	5698	4	0.25	2	1.5	14	PW	8.12	0.57	0.48	1.65	0.7
					9	0.25	2	2.2	62	I	12.3	1.35	0.11	> 20	0.8
9036	2			0.25	2	1.1	6.1	PW	1.86	0.18	0.19	0.33	0.6		
	2			0.10	2	2.1	17	PW	9.55	0.74	0.19	3.38	0.6		
	2			0.00	2	4.9	22	I	13.8	0.95	0.00	> 20	0.6		
	4			0.25	2	1.5	13	PW	4.68	0.61	0.72	1.41	0.7		
	4			0.10	2	2.6	32	I	11.7	1.05	0.04	> 20	0.7		

TAB. 2